International Symposium
On Turbulence and Shear Flow
Phenomena (TSFP-9)
June 30 - July 3, 2015 *Melbourne, Australia*

THE FLOW FIELD INSIDE A RANQUE-HILSCH VORTEX TUBE PART II: TURBULENCE MODELLING AND NUMERICAL SIMULATION

Christian Morsbach[1], **Daniel Schlüß**[1], **Martin Franke**[2]
Department of Numerical Methods
Institute of Propulsion Technology, German Aerospace Center (DLR)
[1]Linder Hoehe, 51147 Cologne, Germany; [2]Mueller-Breslau-Str. 8, 10623 Berlin, Germany
christian.morsbach@dlr.de

Ulrich Doll, Eike Burow, Manfred Beversdorff, Guido Stockhausen, Christian Willert
Department of Engine Measurement Systems
Institute of Propulsion Technology, German Aerospace Center (DLR)
Linder Hoehe, 51147 Cologne, Germany

ABSTRACT

The flow in a Ranque-Hilsch vortex tube was investigated using turbulence models of different closure levels ranging from linear eddy viscosity over explicit algebraic Reynolds stress to differential Reynolds stress models. Unsteady flow features could be resolved with the differential Reynolds stress model. The results were validated against experimental data reported in part I of this paper and show qualitative as well as quantitative agreement. A detailed analysis of the flow topology as well as unsteady effects is presented.

INTRODUCTION

The Ranque-Hilsch vortex tube (RHVT) is a fluid mechanical device used to generate one hot and one cold stream of fluid from one incoming stream of constant temperature. It was first introduced by Ranque (1933) and improved in efficiency by Hilsch (1947). The physical mechanisms behind the thermal separation effect are still a matter of scientific debate (Eiamsa-ard & Promvonge, 2008). Many publications exist that deal either with experimental (e.g. Liew *et al.*, 2012) or numerical investigations of vortex tubes. Secchiaroli *et al.* (2009) investigated a RHVT employing RANS as well as LES approaches. Comparisons between experiments and numerical results are rather scarce and mostly restricted to global data such as temperature separation (e.g. Baghdad *et al.*, 2011). In a joint project of the departments of Engine Measurement Systems and Numerical Methods at DLR's Institute of Propulsion Technology the vortex tube is investigated both experimentally and numerically. With the focus of the project on RANS turbulence model validation, high quality data of the flow within the RHVT are obtained by optical measurement techniques such as Laser-2-Focus (L2F, Schodl, 1980) and filtered Rayleigh scattering (FRS, temperature, pressure, Doppler shift). Details on the global characterisation, pressure and FRS measurements can be found in the first part of this paper (Doll *et al.*, 2015).

The flow in the experimentally investigated vortex tube is simulated using turbulence models of different closure levels to gain insight into their performance in complex flow topologies. Due to the unsteady nature of the flow, which was observed experimentally, steady as well as unsteady RANS simulations were performed and evaluated. After an assessment of the prediction quality by comparison with experimental data, the focus of this paper is on the analysis of the flow topology and unsteady effects in the vortex tube.

NUMERICAL METHOD AND TEST CASE

The numerical analysis was conducted using DLR's in-house flow solver for turbomachinery applications TRACE (Becker *et al.*, 2010). TRACE is a density-based, compressible RANS solver based on the finite volume method. The turbulence model transport equations are solved in a segregated and conservative manner (Morsbach & di Mare, 2012). Steady state solutions are obtained by an implicit pseudo-time stepping algorithm for which the turbulence source terms have been linearised (Morsbach *et al.*, 2015). The unsteady RANS simulations were conducted using a second order time accurate backward difference scheme, for which the inner iterations are solved with the same pseudo-time method as in the steady simulation.

As a well-established reference model the linear eddy viscosity Menter SST k-ω model (Menter *et al.*, 2003) was chosen. However, the Boussinesq assumption is bound to fail in complex flows with highly anisotropic turbulence. It is, therefore, desirable to apply more general approaches such as differential Reynolds stress models (DRSM). In this case, the high Reynolds SSG/LRR-ω DRSM by Eisfeld (2010) was used. The model combines the LRR pressure-strain model in boundary layers with the SSG model in free shear layers. It has been shown to produce reasonably accurate results in complex aerodynamic flows even compared to more sophisticated low Reynolds models (Morsbach *et al.*, 2015). For stability reasons, a simple instead of a generalised gradient diffusion hypothesis was employed

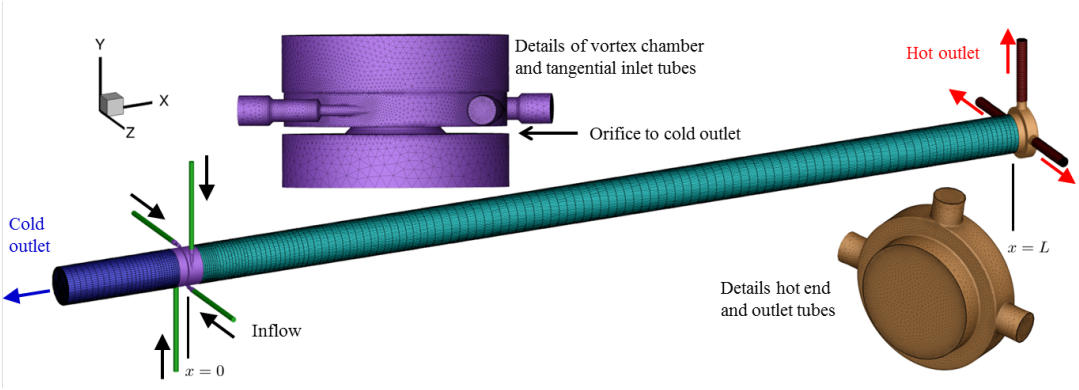

Figure 1. Geometry of Ranque-Hilsch vortex tube and mesh details of vortex chamber and hot end.

for the Reynolds stress equations since the diffusion model was shown to have only limited influence in complex flows (Eisfeld, 2014). Especially for industrial applications, explicit algebraic Reynolds stress models (EARSM) are an attractive compromise between the accuracy of a full differential Reynolds stress closure and the robustness of a linear eddy viscosity model. Therefore, the performance of the Hellsten EARSM k-ω model (Hellsten, 2005) in this flow was evaluated additionally. All turbulence models employ a constant turbulence Prandtl number approach for the turbulent heat flux.

The geometry of the RHVT is given by the experimental set-up described in the first part of this paper. The tube is $L = 700\,\text{mm}$ long and its radius amounts to $R = 15\,\text{mm}$. The origin of the coordinate system is on the axis of the vortex tube in the plane of the inflow tubes. To ensure comparability with the experiments, most geometrical details were considered in the simulation. This could only be achieved with reasonable effort by choosing an unstructured mesh topology. All boundary layers were meshed with either hexahedral elements in the pure cylindrical parts of the geometry or with prism elements in the geometrically complex connection regions, i.e. the vortex chamber and the hot end. The non-dimensional distance of the first cell centre from solid walls was ensured to be around $y^+ \sim 0.5$ in the vortex chamber, main tube and hot end and around $y^+ \sim 1$ in the remaining parts. The remaining volume is filled with tetrahedra. This procedure resulted in a total number 5.8 million cells. Fig. 1 shows the geometry and the mesh used in all subsequent investigations.

A mesh study was performed using three meshes differing mainly in the stretching rate and number of boundary cell layers. As a result of that, the spatial resolution of the tetrahedra filling the volume is varied. The first distance from the wall, however, was held constant to ensure the correct low Reynolds wall boundary condition. The coarse and fine meshes consist of 4.0 and 12.6 million cells, respectively.

The operating point is defined by the fraction of mass flow exiting the device through the cold outlet $\varepsilon = \dot{m}_{\text{cold}}/\dot{m} = 0.3$ termed cold fraction. Air at a total pressure of $p_t = 7\,\text{bar}$ and $T_t = 293\,\text{K}$ is injected through four critical nozzles attached tangentially to the vortex chamber. The swirling flow in the outer region moves toward the hot outlet, where hot air can exit the vortex tube radially. In the inner region, fluid is transported back towards the orifice in the vortex chamber, where it can exit the device axially. At the cold outlet, a constant pressure boundary condition is

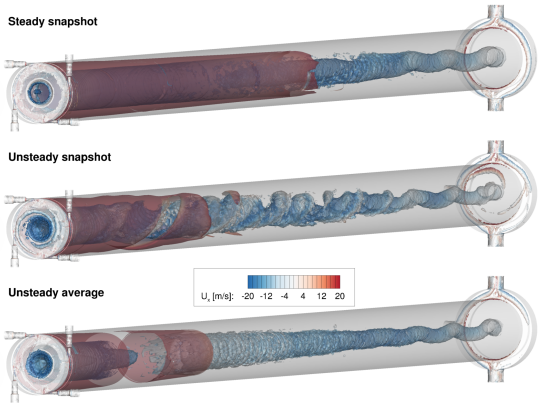

Figure 2. Vortex visualisation by isosurface at $\lambda_2 = -1$ for SSG/LRR-ω model: steady snapshot (*top*), unsteady snapshot (*middle*), unsteady average (*bottom*).

applied whereas a mass flow boundary condition controlling the pressure is set at the three hot outlet boundaries.

In an unsteady RANS simulation, the time step has to be chosen such that the unsteady phenomena of interest can be resolved. Since the vortex tube has no moving parts the characteristic frequencies are determined by the flow only. One measure is the frequency based on the circumferential velocity and the radius of the tube. It varies from about 5000 Hz in the vortex chamber to about 500 Hz at the hot end of the tube. The time step size Δt is chosen such that the highest frequency is resolved with about 100 time steps. To reduce the computation time of the unsteady simulation, the steady result was used to initialise the solver. It was run until the integral boundary data such as mass flow, temperature and pressure showed statistical patterns.

Data sets of different temporal and spatial resolution were recorded in the following time steps. Table 1 summarizes their properties. The 3D data set contains 8 periods of the lowest frequency. One period of the highest fundamental frequency is sampled with at least 12 points. The huge amount of storage required for the 3D data set limits the length of the sample and the sampling rate. Hence, 2D surfaces at different axial positions x/L and the $z = 0$ plane over the complete length of the vortex tube were generated in the pre-process by intersection with the 3D mesh and the flow solution is interpolated to these surfaces on output. Point probes (0D) were introduced at the positions

Table 1. Properties of recorded time series.

Spatial	Length [ms]	Sampling rate [kHz]
3D	16.8	60.8
2D	33.7	121.6
0D	115.6	486.4

of the pressure sensors in the experiment which allowed to record the complete unsteady simulation. The lowest frequency resolved by one period by the 0D data set is about 10 Hz. The full 3D time series was used to gain insight into the global flow topology, whereas the 2D and 0D time series were evaluated in the frequency domain and compared with experimental data. To reduce the computational effort of the FFT, the data from the unstructured 2D mesh were interpolated to a structured rectangular mesh with lower spatial resolution. On this mesh, the FFT was performed for every point in space.

RESULTS AND DISCUSSION

The first step in the interpretation of the results is the evaluation of the influence of the mesh resolution. For this purpose, a steady state computation using the Menter SST k-ω model was performed for each mesh. Radial velocity profiles in the vortex tube near the vortex chamber at $x/R = 1, 2, 4$ as well as averaged temperature data at the outflow boundaries were compared. Velocities on the different meshes varied by about 5 m/s. This amounts to up to 5 % of the circumferential velocity at the investigated stations, while, because of the low velocities in the core region, the relative deviation in axial velocity can be up to 25 %. The averaged temperature varies by about 4 K which corresponds to approximately 1 % in absolute temperature. All following results have to be evaluated considering this uncertainty.

Steady-state solutions of the flow within the RHVT were obtained using the Menter SST k-ω and Hellsten EARSM k-ω models. However, due to the less diffusive nature of DRSMs, no converged steady-state solution could be obtained with the SSG/LRR-ω model in this inherently unsteady case. Fig. 2 shows the flow topology computed with the latter model using a $\lambda_2 = -1$ isosurface. A snapshot of the unsteady RANS solution (*middle*) shows clear evidence of large scale unsteady effects. The vortical structures rotate around the core flow towards the cold outlet. On average (*bottom*), a straight vortex core is detected in the first 70% of the tube, while a helical structure occurs towards the hot end. It is also seen in the steady-state snapshot (*top*) and might, therefore, be attributed to a steady flow feature induced by the asymmetry of the hot end.

Quantitative differences between steady and unsteady results of the SSG/LRR-ω model as well as the Menter SST k-ω and Hellsten EARSM k-ω models are shown in Fig. 3. The predicted axial (*top*) and circumferential (*middle*) velocities U_x and U_z at $x/R = 1$ are compared to experimental data of the mean flow obtained by the L2F method. A local minimum in U_x (flow towards cold outlet) at $y/R = 0.75$ is evident in the experimental data. In contrast, the Menter SST k-ω model predicts monotonously increasing U_x from the centre to the maximum at the edge of the wall boundary

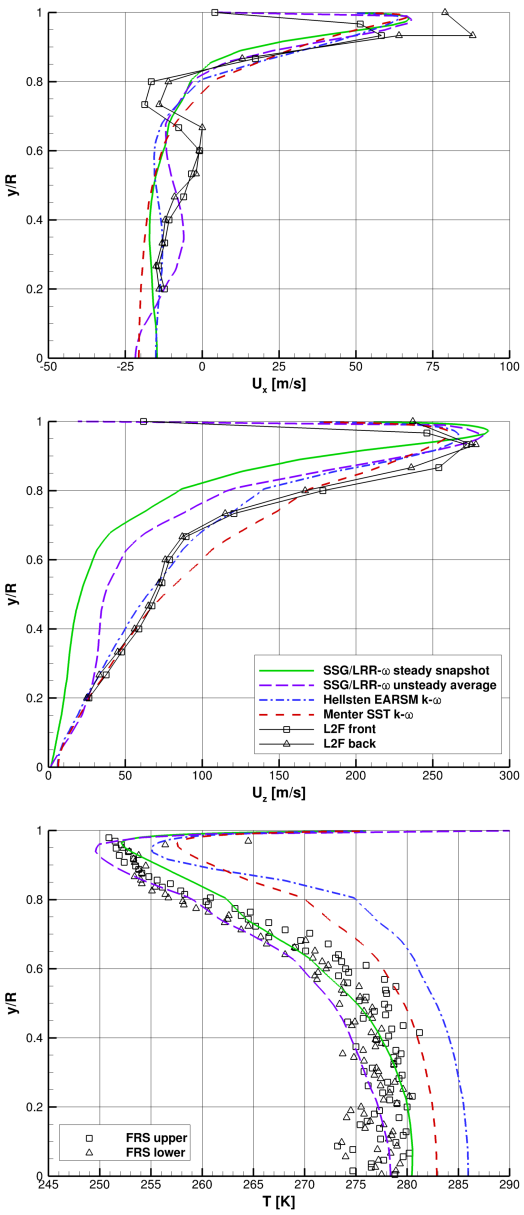

Figure 3. Comparison of axial and circumferential velocity U_x (*top*) and U_z (*middle*) radial profiles with L2F data and temperature T (*bottom*) radial profiles with FRS data at $x/R = 1$.

layer. Anisotropy resolving models seem to be required to produce this S-shape, although it is far less pronounced in the steady Hellsten EARSM k-ω and SSG/LRR-ω solutions than in the experiment. However, when the latter model is used in an unsteady RANS context, a local extremum appears at $y/R \approx 0.7$ in the averaged solution. The second extremum, a local maximum in U_x is found at $y/R \approx 0.35$. Similar conclusions can be drawn for the circumferential velocity U_z. The experimental data confirm the solid body like rotation in the core flow reported by several authors (e.g. Liew *et al.*, 2012) up to $y/R \approx 0.4$. A short region of decreased velocity gradient follows up to $y/R \approx 0.6$. This feature is reproduced by neither the Menter SST k-ω nor the Hellsten EARSM k-ω model. The steady SSG/LRR-

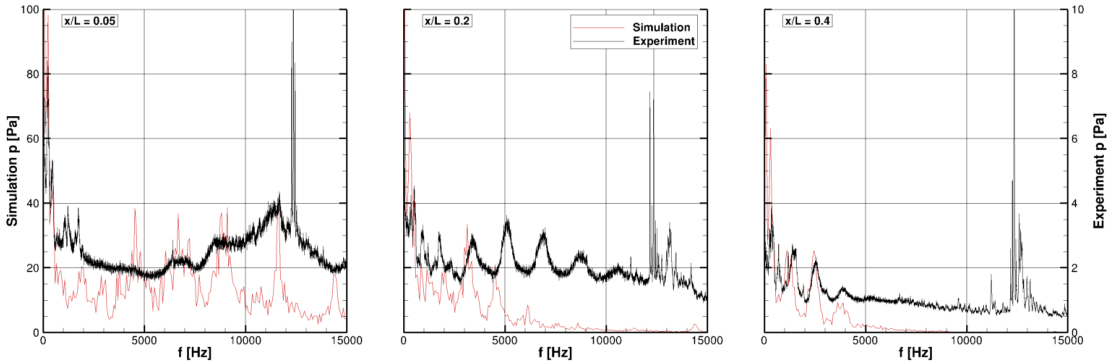

Figure 4. Fourier transform of pressure signal obtained with unsteady computation with SSG/LRR-ω model from 0D data set compared to measured data at $x/L = 0.05, 0.2$ and 0.4.

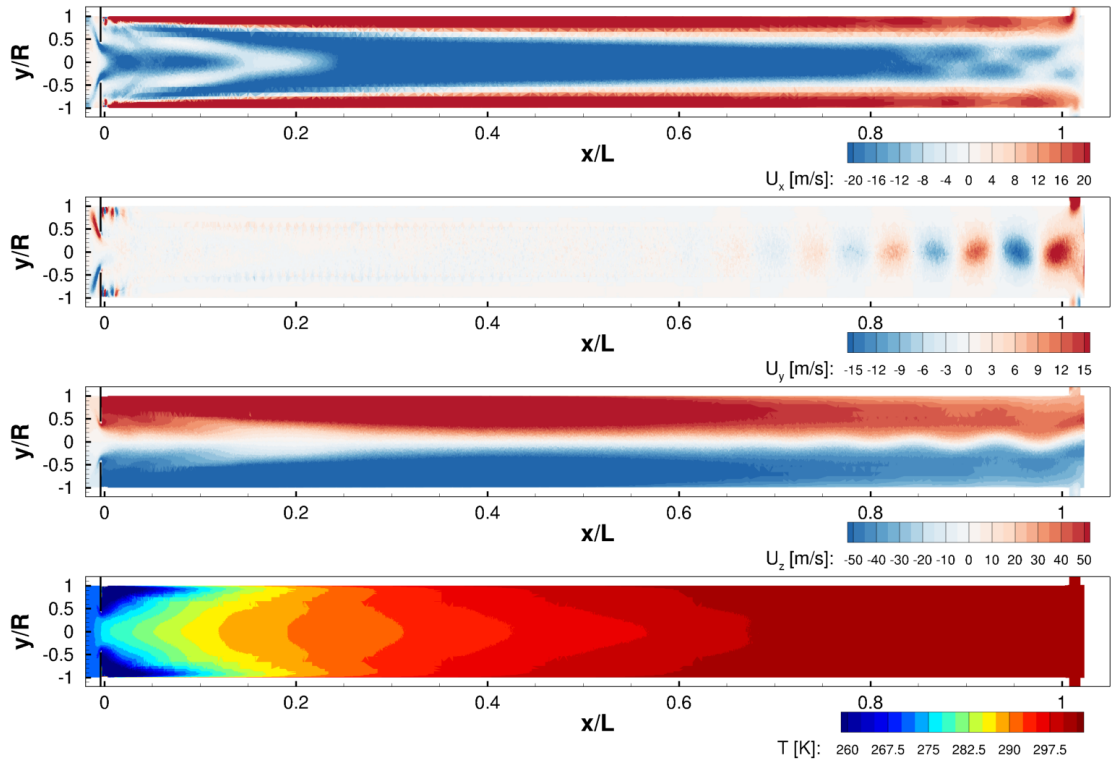

Figure 5. Contours of average velocity components U_x, U_y, U_z and temperature T in the $z = 0$ plane from 2D data set computed with SSG/LRR-ω model.

ω solution dramatically underestimates the gradient in the core region. Only the averaged unsteady solution can reproduce the solid body like rotation followed by the region of reduced gradient. Although the experimental data are not matched quantitatively, the qualitative prediction of the velocity field is improved if the DRSM is applied in unsteady RANS mode.

The measured global temperature separation amounts to $\Delta T = T_h - T_c = 23.8\,\mathrm{K}$. The Menter SST k-ω and the Hellsten EARSM k-ω model underestimate ΔT by 5 K and 12 K respectively. In contrast, ΔT is overpredicted by the SSG/LRR-ω model by 8 K. The trend in ΔT is also expressed in the radial temperature profiles at $x/R = 1$ shown in Fig. 3 (*bottom*). While both Menter SST k-ω and Hellsten EARSM k-ω models overestimate the temperature near the cold outlet by up to 10 K, it can be reproduced by the averaged unsteady solution of the SSG/LRR-ω model.

While the time averaged unsteady solution shows good qualitative agreement with measured time averaged data, it remains to be evaluated if unsteady flow features are resolved accurately. This is done by comparison of pressure signals in the frequency domain at different positions along the vortex tube. The unsteady pressure signal was experimentally recorded by Kulite sensors and transformed to the frequency domain by FFT. Fig. 4 shows the frequency content of the pressure signal at axial positions $x/L = 0.05, 0.2$ and 0.4 measured at the wall of the tube. The experimental data show dominant peaks at a frequency of about 12.5 kHz, which is not present at any station in the numerical results. The spectra also differ at lower frequencies in the first 20 %

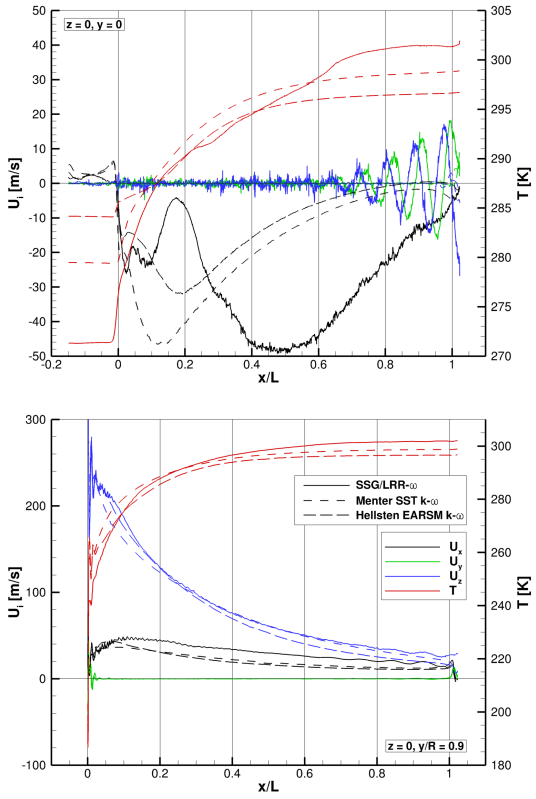

Figure 6. Velocity U_x, U_y, U_z and temperature T profiles in the $z = 0$ plane at $y = 0$ (*top*) and $y/R = 0.9$ (*bottom*) extracted from steady solutions computed with Menter SST k-ω and Hellsten EARSM k-ω models, respectively, and unsteady 2D data set computed with SSG/LRR-ω model.

of the vortex tube. At $x/L = 0.4$, the dominant frequencies and its harmonics correspond to the circumferential velocity at this axial position of the simulation. The experimental data also show peaks at these frequencies.

Fig. 5 shows the averaged velocity components U_x, U_y, U_z and temperature T in the $z = 0$ plane plotted from the orifice to the cold outlet to hot end computed with the SSG/LRR-ω model. For quantitative comparison, profiles at constant $y = 0$ and $y/R = 0.9$ are plotted in Fig. 6. The computed flow in the vortex tube can be divided into three regions distinguished by axial temperature gradient, radial temperature gradient, axial velocity and secondary flow structures. The following analysis attempts to link these observations.

The first region extends from the cold outlet to approximately $x/L = 0.25$. There, the radial temperature minimum can be found at about $y/R = 0.95$ instead of the core region resulting from the expansion of the injected gas. At all radial positions, the axial temperature gradient is at its maximum value in this part of the vortex tube. The region exhibits a conical structure of nearly vanishing negative axial velocity. It is confirmed experimentally by the L2F measurements as shown in Fig. 3 for a single axial position $x/R = 1$. This local axial velocity extremum does not occur beyond $x/L > 0.15$. The direct effects of the injection play a major role in the flow topology up to about $x/L = 0.025$. Fluctuating horse shoe vortices develop around the four jets injected into the vortex chamber.

The second region is characterised by a moderate axial temperature gradient from $x/L = 0.25$ to $x/L = 0.65$. At the beginning of the region at $x/L = 0.25$ the temperature minimum moves from the outer region to the core region. From there to the hot end, the radial temperature minimum can be found at $y = 0$. While the axial and circumferential velocities decay monotonously in the peripheral region, the axial velocity in the core reaches its greatest negative value at $x/L = 0.5$. No significant secondary flow structures develop in this region.

From $x/L = 0.65$ to the hot end, the axial temperature gradient tends to and reaches zero at about $x/L = 0.9$. At $y = 0$, the axial velocity linearly tends to zero. Secondary flow structures start to develop and manifest themselves as the helical structure of the λ_2 iso surface (Fig. 2). They can be seen in all velocity components in Fig. 5. Towards the hot end the intensity of the vortices mixing the core flow with the peripheral flow increases. Fig. 6 clearly shows increasing amplitudes of the oscillations in U_y and U_z at $y = 0$. Due to the enhanced convective mixing of fluid, also the radial temperature gradient nearly vanishes. It cannot be definitely concluded within this study if this is a flow feature due to the asymmetry of the hot outlet configuration or a general feature of the vortex tube.

The steady state results obtained with the Menter SST k-ω and Hellsten EARSM k-ω models are plotted in Fig. 6 for comparison. At $y/R = 0.9$ they only differ quantitatively from the averaged results obtained with the unsteady SSG/LRR-ω simulation. The temperature rises quicker while the axial velocity decays faster and both quantities reach a nearly constant level at about $x/L = 0.5$. On the centreline, however, the velocity and temperature fields differ qualitatively. No region of partial stagnation is predicted by the steady simulations. In the (unconverged) steady simulation using the SSG/LRR-ω model, however, this region can be detected, hinting that a DRSM is required to predict this flow feature. Furthermore, neither the LEVM nor the EARSM predict secondary flow structures or the linear decay of axial velocity at the hot end.

To gain further insight into the unsteady behaviour of the flow, the data in the frequency domain were analysed with higher spatial resolution. At the radial positions $y/R = 0$ and 0.9, a FFT of the unsteady time signal is performed over the whole axial range. Fig. 7 shows the amplitude of the circumferential velocity signal dependent on axial position and frequency. Liew *et al.* (2012) argue that the dominant frequency in their unsteady velocity signal correlates with the maximal vorticity. For this reason, the frequency $f = U_{z,\max}/2\pi r_{\max}$ of the main vortex is computed at discrete stations $x/L \in [0.03, 0.97]$. The resulting base frequency f_0 and its first two harmonics f_1 and f_2 are also plotted in Fig. 7. In the outer tube ($y/R = 0.9$, bottom), all three frequencies are dominant over large parts of the vortex tube. They correspond to the maximal circumferential velocity at the respective axial position. Especially in the vortex chamber, where the high pressure gas is injected into the tube, the two harmonics dominate. On the axis ($y/R = 0$, top), however, only the base frequency has a significant contribution. This supports the experimental findings of Liew *et al.* (2012), who stated that contributions to the base frequency are found mainly on the centre line while higher harmonics become visible at greater radii.

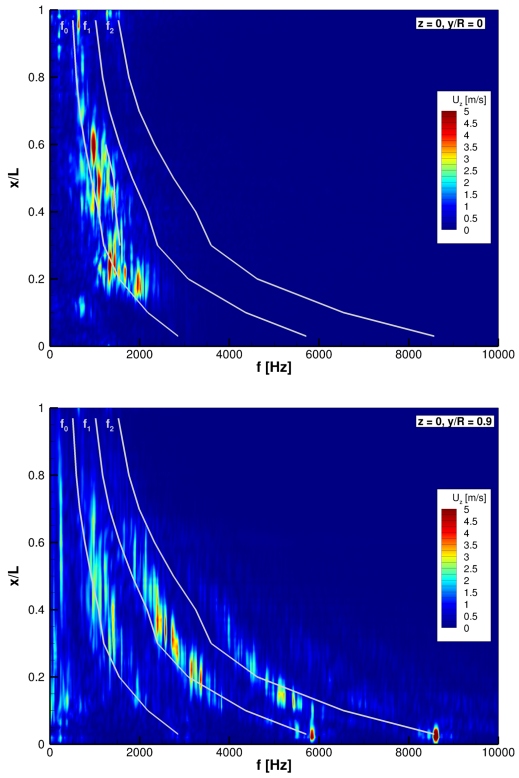

Figure 7. Fourier transform of circumferential velocity U_z at $z = 0$ on axis (*top*) and at $y/R = 0.9$ (*bottom*) from 2D data set computed with SSG/LRR-ω model.

CONCLUSION

The flow within a RHVT was investigated using turbulence models of different closure levels. All models were able to predict the effect of temperature separation. With regard to velocity profiles measured by L2F, it was shown that an unsteady simulation using the SSG/LRR-ω DRSM produced the best qualitative results, while quantitative agreement with measured temperature data could be improved. Only the DRSM predicted secondary flow structures at the hot end. While the expansion of the injected gas is the main driver for temperature separation, turbulence and unsteady effects do have a non-negligible influence on its magnitude.

Considering the FRS measurements from part I, good qualitative and quantitative agreement of velocities and qualitative agreement of temperature between experiment and numerics employing the DRSM could be obtained in the outer region of the vortex tube. Qualitative differences appear in the inner region, where a strong influence of acoustic phenomena on the mean flow field was found in the experiment. The fact that the simulation, which did not resolve acoustics, predicted temperature separation indicates that coupling between acoustics and the flow field cannot be the only driver for temperature separation.

REFERENCES

Baghdad, Mohammed, Ouadha, Ahmed, Imine, Omar & Addad, Yacine 2011 Numerical study of energy separation in a vortex tube with different RANS models. *International Journal of Thermal Sciences* **50** (12), 2377 – 2385.

Becker, Kai, Heitkamp, Kathrin & Kügeler, Edmund 2010 Recent progress in a hybrid-grid CFD solver for turbomachinery flows. In *V European Conference on Computational Fluid Dynamics ECCOMAS CFD 2010*. Lisbon, Portugal.

Doll, Ulrich, Burow, Eike, Beversdorff, Manfred, Stockhausen, Guido, Willert, Christian, Morsbach, Christian, Schlüß, Daniel & Franke, Martin 2015 The flow field inside a Ranque-Hilsch vortex tube part I: Experimental analysis using planar filtered Rayleigh scattering. In *Ninth International Symposium on Turbulence Shear Flow Phenomena (TSFP-9)*. Melbourne, Australia.

Eiamsa-ard, Smith & Promvonge, Pongjet 2008 Review of Ranque-Hilsch effects in vortex tubes. *Renewable and Sustainable Energy Reviews* **12** (7), 1822 – 1842.

Eisfeld, Bernhard 2010 Reynolds stress modelling for complex aerodynamic flows. In *V European Conference on Computational Fluid Dynamics ECCOMAS CFD 2010*. Lisbon, Portugal.

Eisfeld, Bernhard 2014 The influence of the diffusion model on the separation sensitivity of differential Reynolds stress models. In *New Results in Numerical and Experimental Fluid Mechanics IX* (ed. Andreas Dillmann, Gerd Heller, Ewald Krämer, Hans-Peter Kreplin, Wolfgang Nitsche & Ulrich Rist), *Notes on Numerical Fluid Mechanics and Multidisciplinary Design*, vol. 124, pp. 113–121. Springer International Publishing.

Hellsten, A. 2005 New advanced k-ω tuburlence model for high-lift aerodynamics. *AIAA J.* **43** (9), 1857–1869.

Hilsch, R. 1947 The use of the expansion of gases in a centrifugal field as cooling process. *Review of Scientific Instruments* **18**, 108–113.

Liew, R., Zeegers, J.C.H., Kuerten, J.G.M. & Michałek, W.R. 2012 3D velocimetry and droplet sizing in the Ranque-Hilsch vortex tube. *Experiments in Fluids* **54** (1).

Menter, F., Kuntz, M. & Langtry, R. 2003 Ten years of industrial experience with the SST model. In *Turbulence, Heat and Mass Transfer 4* (ed. K. Hanjalić, Y. Nagano & M. Tummers).

Morsbach, Christian, Franke, Martin & di Mare, Francesca 2015 Application of a low reynolds differential Reynolds stress model to a compressor cascade tip-leakage flow. In *Differential Reynolds Stress Modeling for Separating Flows in Industrial Aerodynamics* (ed. Bernhard Eisfeld), pp. 1–17. Springer International Publishing.

Morsbach, Christian & di Mare, Francesca 2012 Conservative segregated solution method for turbulence model equations in compressible flows. In *6th European Congress on Computational Methods in Applied Sciences and Engineering (ECCOMAS 2012)*. Vienna, Austria.

Ranque, G. J. 1933 Expériences sur la détente giratoire avec productions simultanées d'un echappement d'air chaud et d'un echappement d'air froid. *Journal de Physique et Le Radium* **4** (7), 112–114.

Schodl, R. 1980 A laser-two-focus (l2f) velocimeter for automatic flow vector measurements in the rotating components of turbomachines. *Journal of Fluids Engineering, Transactions of the ASME* **102** (4), 412–419, cited By (since 1996)10.

Secchiaroli, A., Ricci, R., Montelpare, S. & D'Alessandro, V. 2009 Numerical simulation of turbulent flow in a Ranque-Hilsch vortex tube. *International Journal of Heat and Mass Transfer* **52** (23–24), 5496 – 5511.